Real-time Control of Dendritic Propagation in Rechargeable Batteries using Adaptive Pulse Relaxation

Asghar Aryanfar [†][*], Yara Ghamlouche [†], William A. Goddard III [§]

† *American University of Beirut, Riad El-Solh, Lebanon 1107 2020*
‡ *Bahçeşehir University, 4 Çırağan Cad, Beşiktaş, Istanbul, Turkey 34353*
§ *California Institute of Technology, 1200 E California Blvd, Pasadena, CA 91125*

Abstract

The non-uniform growth of the microstructures in dendritic form inside the battery during prolonged charge-discharge cycles causes short-circuit as well as the capacity fade. We develop a feed-back control framework for the real-time minimization of such microstructures. Due to accelerating nature of the branched evolution, we focus on the early stages of growth, identify the critical ramified peaks and compute the effective time for the dissipation of ions from vicinity of those branching fingers. The control parameter is a function of the maximum interface curvature (i.e. minimum radius) where the rate of run-away is the highest. The minimization of total charging time is performed for generating the most packed microstructures which correlate closely with those of considerably higher charging periods, consisting of constant and uniform square waves. The developed framework could be utilized as a smart charging protocol for the safe and sustainable operation of rechargeable batteries, where the branching of the microstructures could be correlated to the sudden variation in the current/voltage.

Keywords: Pulse Relaxation, Interface Curvature, Dendritic Growth, Real-time Optimization.

1   Introduction

The growing demand for portable computational power requires novel and reliable high capacity energy storage devices. Despite such impressive growth of the need in the daily lifestyle, the underlying science remains to be developed [1]. Rechargeable batteries, which retrieve/store energy from/within the chemical bonds, have proven to be the most reliable and cleanest resource of electrical energy for efficient power management [2, 3].

---

[*]Corresponding author; email: aryanfar@caltech.edu

It is well established that Lithium is the ideal metal used for anodes in batteries because of their possession of a very high specific capacity (372 $mAh.g^{-1}$) and the lowest redox potential (-3.04 V relative to standard hydrogen electrode) [4]. Although the development of portable electronics, electric vehicles and wireless devices is in continuous acceleration, their main source of energy storage – the Li rechargeable batteries – is still facing some challenges. Li-batteries are still far from providing safe and efficient applications due to their low Coulombic efficiency and their dendritic growth [5]. Deposition behavior of Li atoms is one major barrier in front of rechargeable batteries' development and efficiency [6]. During electrodeposition, the ions do not shape a flat surface and form sharp dendritic structures instead because they are very highly reactive metals [7, 8]. The dendritic morphology of the surface leads to internal short circuits (when the ions reach the cathode) which might then cause critical thermal runaway for the batteries as well as fast anode capacity fading [4, 6, 9, 10]. This happens more frequently when the charging is fast which causes complications in all practical applications of the batteries [8]. Hence the need for efficient methods to ensure the suppression of the dendrites. Many approaches have been developed for this purpose including mechanical suppression with solid-solid interfaces [9], placement of the Li ions in a scaffold [11], addition of electrolyte additive [12] or alloying additional composites on the Li foil to control stripping [13].

During charge period, the fast-pace formation of microstructures with relatively low surface energy from Brownian dynamics, leads to the branched evolution with high surface to volume ratio [14]. The speeding evolution of microstructures makes them highly branched and porous. This helps them unnecessarily occupy a large volume for a small amount of charge, possibly reaching the counter-electrode and short-circuit the cell. Additionally, they can also dissolve from their thinner necks during subsequent discharge period and form detached dead crystals. This leads to thermal instability and capacity decay [15]. Such a formation-dissolution cycle is particularly prominent for the metal electrodes due to lack of intercalation, which is the diffusion into inner layer as the housing for the charge, where the depositions on the surface is the only dominant formation mechanism versus the diffusion into the inner layers as the housing [16]. The growing amorphous crystals could pierce into the polymer electrolyte and shorten the cell. Given their higher porosity, they could have mechanical properties comparable to the bulk form [17].

Previous studies have investigated various factors of dendrites formation such as current density [18], electrode surface roughness [19, 20], impurities [21], solvent and electrolyte chemical composition [22, 23], adhesive polymers[24], temperature [25, 26], guiding scaffolds [27, 28], capillary pressure [29], cathode morphology [30] and mechanics [31, 32, 33, 34]. Some of the conventional characterization techniques used include NMR [35] and MRI. [36] Recent studies have also shown the necessity of the stability of the solid electrolyte interphase (i.e. SEI) layer for controlling the nucleation and growth of the branched medium [37, 38] as well as pulse charging [39, 40].

Previous models of dendrites had focused on the electric field and space charge as the main responsible mechanisms [41]. The later models focused on ionic concentration causing the diffusion limited aggregation (DLA) [42, 43]. Both mechanisms are part of the electrochemical potential [44], indicating

that each could be dominant depending on the localization of the electric potential or ionic concentration within the medium. Recent studies have explored both factors and their interplay, particularly in continuum scale and coarser time intervals, matching the scale of the experimental time and space [45]. Other simplified frameworks include phase field modeling [46, 47, 48] and analytical developments [49].

During the charging phase, the ions accumulate at the dendrites tips (unfavorable) due to high electric field on the convex boundary. At the same time, they tend to diffuse away to the other less-concentrated regions due to diffusion (favorable). Such dynamics typically occurs within the double layer (or stern layer [50]) which is relatively small and comparable to the Debye length. At high charge rates, the ionic concentration is depleted on the reaction sites and could tend to zero [51]; Nonetheless, our continuum-level study extends to larger scale, beyond the double layer region [52].

Dendrites instigation is rooted in the non-uniformity of electrode surface morphology at the atomic scale combined with Brownian ionic motion during electrodeposition. Any asperity in the surface provides a sharp electric field that attracts the upcoming ions as a deposition sink. Indeed the closeness of a convex surface to the counter electrode, as the source of ionic release, is another contributing factor. In fact, the same mechanism is responsible for the further semi-exponential growth of dendrites in any scale.

Pulse method has been qualitatively proved as a powerful approach for the prevention of dendrites [45], which has previously been utilized for uniform electroplating [53]. The pulse method consists of two consecutive periods: the charging period t_{ON} during which the current is supplied and the subsequent rest period t_{OFF} where the applied current is zero. During the charge the mass flux to-and-away from a given region cooperatively with the rate of depleting reduction reaction determines the ultimate concentration of ions. While the reaction can occur in any surface, it is highly probable in the tips due to high electric fields. During the subsequent relaxation period, these ions spread out and leave towards low-concentrated zones, providing the equilibrium state where ideally afterwards the net diffusion due to Brownian motion is zero. The optimum rest period is in fact the RC time of the electrochemical system [45, 54], similar to the relaxation scale of the blocking electrodes. We have explained qualitatively how relatively shorter pulse periods with identical duty cycles **D** reduces the dendrites. The coarse grained computationally-affordable algorithm allows reaching the experimental time scale (ms). We have developed theoretical limit the optimal minimization of the dendrites [40] and we have obtained the pulse charging parameters for individual curved peaks based on their curvature [52].

In this paper, we elaborate on the real-time controlling of the pulse relaxation parameters for the minimization of microstructures grown in the scales extending to the cell domain, while minimizing the charging time. Such development is based on the radius of the curvature of the critical site in the interface. The response of the imposed relaxation time to the formation of curved surface is shown to be extremely agile. Ultimately we compare the resulted morphology with imposing various constant relaxation periods.
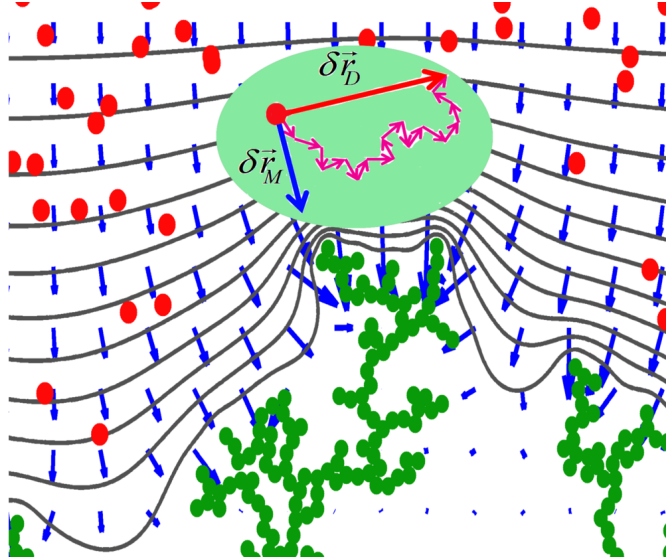
Figure 1: Snapshot of the Dendritic growth simulation with the transport elements. green: dendrite, red: free ions, blue: electric field, gray: iso-potential contours. The green oval contains the displacement vectors.)

2 Methodology

During a typical charge period, the ionic species Li^+ get transported across the cell due to electrochemical flux and get reduced to the atomic form via the the following reaction:

$$Li^+ + e^- \rightarrow Li^0 \tag{1}$$

The electrochemical flux is generated either from the gradients of concentration (∇C) or electric potential (∇V). At the ionic scale, the ions of the higher concentration regions tend to collide with and repel from each other more and, given enough time, diffuse to lower concentration zones, following Brownian motion. In the continuum (i.e. coarse) scale of time, such inter-collisions could be added-up and be represented by the diffusion length $\delta \vec{\mathbf{r}}_D$ as: [45]

$$\delta \vec{\mathbf{r}}_D = \sqrt{2D\delta t}\ \hat{\mathbf{g}} \tag{2}$$

where $\vec{r}_D$ is diffusion displacement of individual ion, D is the ionic diffusion coefficient in the electrolyte, δt is the coarse time interval , and $\hat{\mathbf{g}}$ is a normalized vector in random direction, representing the Brownian dynamics. The diffusion coefficient D is generally concentration dependent [39], due to electro-neutrality within the considerable space in the domain and we assume it is constant in the range considered. The diffusion length represents the average progress of a diffusive wave in a given time, obtained directly from the diffusion equation[55]. δt is in fact the coarse grained time scale, which approximates the displacement wave from many inter-collisions in the smaller time scales (i.e. fs).

On the other hand, ions tend to acquire drift velocity in the electrolyte medium when exposed to electric field and during the given time δt their progress $\delta \vec{\mathbf{r}}_M$ is given as:

$$\delta \vec{\mathbf{r}}_M = \mu \vec{\mathbf{E}} \delta t \tag{3}$$

where μ is the mobility of cations in electrolyte, $\vec{\mathbf{E}}$ is the local electric field. The voltage V is obtained from the laplacian relationship.

Therefore the total effective displacement $\delta \vec{\mathbf{r}}$ would be:

$$\delta \vec{\mathbf{r}} = \delta \vec{\mathbf{r}}_D + \delta \vec{\mathbf{r}}_M \tag{4}$$

as represented in the Figure 1 and the potential of each ion is considered to be the average of the grid that the ion falls in. Since the Rayleigh number Ra is highly correlates with the thickness (i.e. $Ra \propto l^3$), for a thin layer of electrodeposition we have $Ra < 1500$ and thus the convection is negligible [56].

Assuming electro-neutrality in the domain one has [57]:

$$\nabla^2 V \approx 0 \tag{5}$$

where the dendrite body is part of the boundary condition per se and the double layer region has been omitted due to small effect [45]. Equation 5 in 2D translates into the following:

$$\frac{\partial^2 V}{\partial x^2} + \frac{\partial^2 V}{\partial y^2} \approx 0 \tag{6}$$

The Equation 6 can be solved using the finite difference scheme. Assuming that $V_{i,j}$ represents the electric potential value in the location (x_i, y_j) one has:

$$\frac{V_{i+1,j} - 2V_{i,j} + V_{i-1,j}}{\delta x^2} + \frac{V_{i,j+1} - 2V_{i,j} + V_{i,j-1}}{\delta y^2} \approx 0 \tag{7}$$

Assuming the segmentations in the horizontal and vertical directions are identical ($\delta x = \delta y$) this Equation can be re-organized as:

$$V_{i,j} = \frac{1}{4}\left(V_{i+1,j} + V_{i-1,j} + V_{i,j+1} + V_{i,j-1}\right) \tag{8}$$

which means that the value at each given coordinate $V_{i,j}$ equals the average of the four first order neighbors surrounding it. The boundary condition for solving equation 8 is the potential values in the counter-electrodes as well as the dendrites:

$$\begin{cases} V_{anode} = V_- \\ V_{cathode} = V_+ \\ V_{dendrite} = V_- \end{cases} \tag{9}$$

As well the periodic boundary condition is applied on the ions leaving the domain. Therefore, the
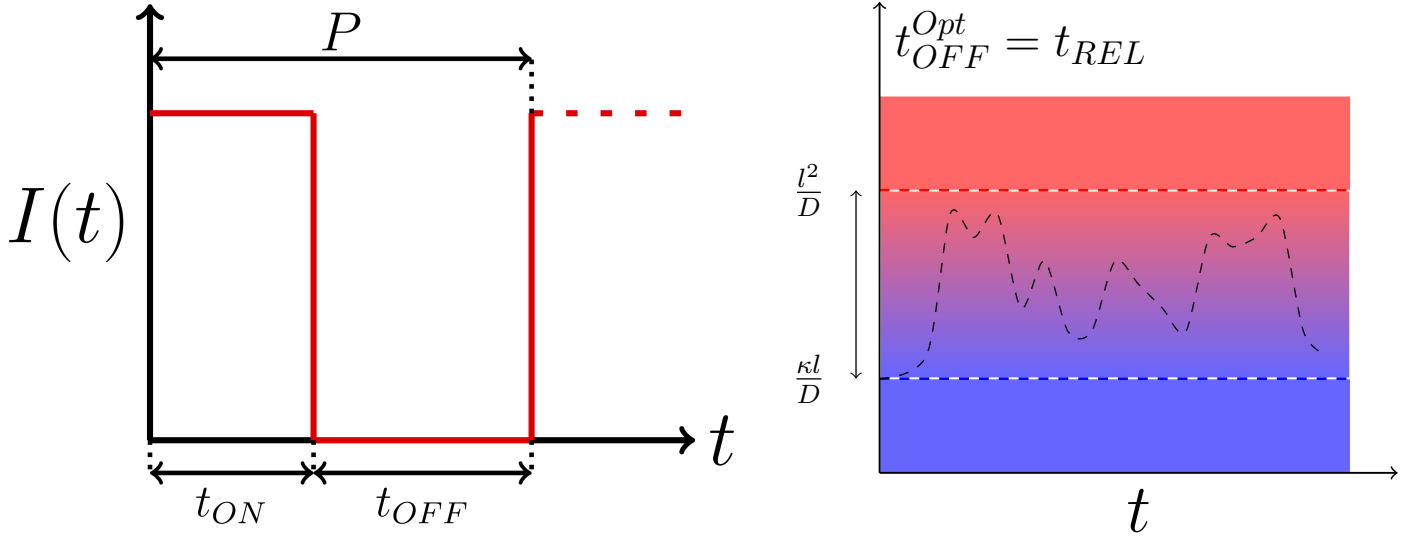
(a) Square pulse wave by the amount of current applied $I(t)$ in time.

(b) Schematics of the variation in the feedback relaxation time t_{REL} in the range of shown boundaries, depending on the interface curvature r_d.

Figure 2: Time-dependent parameters: t_{REL} is used as a control parameter for dendritic suppression.

Equation 8 can be solved for any given point via iteration of the potential values until the results of the successive iterations converge. Needless to mention that the potential value in the dendrite body is the same as the anode since they are physically connected as shown in the Equation 9. Consequently, the electric field is the gradient of electric potential as:

$$\vec{\mathbf{E}} = -\nabla V \tag{10}$$

The initial layer is defined as a line of atoms in the bottom of the domain. During the simulation, the upcoming ions gradually move toward the electrode due to electric field and approach to the electrode surface. If there is overlap in volume, the reaction 1 occurs with an specific probability and the ion joins the dendrite body, leading to the growth.

The pulse charging in its simplest form consists of trains of square active period t_{ON}, followed by a square rest interval t_{OFF} in terms of current I or voltage V as shown in Figure 2a. The period $P = t_{ON} + t_{OFF}$ is the time lapse of a full cycle. Hence the pulse frequency f is:

$$f = \frac{1}{t_{ON} + t_{OFF}} \tag{11}$$

and the duty cycle $\mathbf{D}$ represents the fraction of time in the period P that the pulse is active:

$$\mathbf{D} = \frac{t_{ON}}{t_{ON} + t_{OFF}} \tag{12}$$
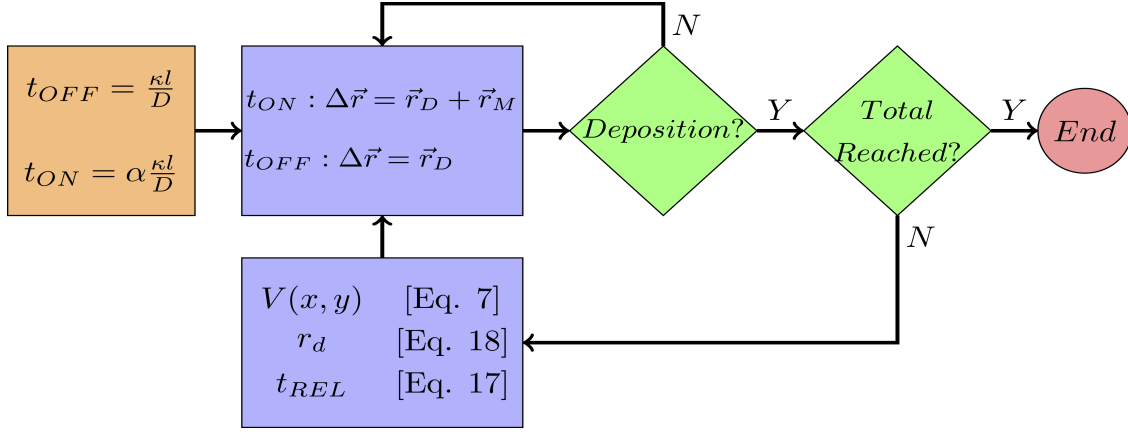
$$= f t_{ON} \tag{13}$$

Figure 3: Pseudo-chart of the feedback algorithm.

During the growth process, the dendritic branches evolve in random directions due to Brownian nature of ionic motion and deposition. The formed fingers possess a high curvature and have closer proximity to the upcoming ions. Thus they develop excessive amount of electric field in their tips which becomes a source for the acceleration in their development per se. Hence imposing a relaxation time would allow the concentrated ions in the ramified peaks to dissipate away into the less-concentrated regions - likely into the pores inside the dendrite - until the formation of uniform concentration of ions across the dendrite. The time required for this relaxation depends on the curvature of the interface, where the higher curvature sites would require a shorter time for the concentration relaxation within the double layer region [52]. In fact such relaxation could occur locally within interfacial double layer scale the thickness of κ to globally within the span of the entire cell domain. From dimensional analysis, the relaxation time of the double layer in the flat electrode is in the range of $\sim \dfrac{\kappa^2}{D}$ [58] and for the larger domain of the cell with the representative length of l, it would scale up to $\sim \dfrac{l^2}{D}$. Their geometric mean has been later considered as $\sim \dfrac{\kappa l}{D}$ [54]. In fact the relaxation of the concentration depends highly on the curvature of the peaks. The entire growing interface possesses a wide range of radius of curvature values r_d, expanding from the flat surface to the highly-curved fingers as small as the atomic value, therefore:

$$r_d \in [a, \infty) \tag{14}$$

Hence, the relaxation time for a randomly-growing interface with variation of curvature along the interfacial line, would vary as well. Hereby, we define the feedback relaxation time t_{REL} a curvature dependent function $f(r_d)$ multiplied by the geometric mean time for the concentration relaxation (i.e. RC time) as:

$$t_{REL} = f(r_d)\frac{\kappa l}{D} \tag{15}$$

As the interface grows from the initial flat state ($r_d \to \infty$) to ultimately creating sharp fields

7

($r_d \to a$), the feedback relaxation time t_{REL} should adapt respectively based on the most critical state of the interface, which is the location of ionic concentration. During the initial stage of dendritic growth the concentration gradient only exists in the double layer region ($\sim \kappa$) and therefore the relaxation in those sites would suffice for the uniform growth. After initiation of the peaks and the accumulation of the ions in the ramified zones, the relaxation should occur in consideration of the entire scale of the domain ($\sim l$). Hence, the feedback relaxation time t_{REL} should occur from its minimal value during the instigation, to its maximal value in the atomic scale.

An appropriate measure of the degree of formation of peaks in the growing dendritic morphology is their respective radius of curvature r_d.

In order to prevent the excessive growth of the peaks and to get uniform morphology one needs to provide enough relaxation time to diffuse away the concentrated ions in the tips. While the relevant relaxation time-scale for the uniformization of the concentration gradient in the flat interface is $\sim \dfrac{\kappa l}{D}$, the extreme peaks might require the uniformization up to the scale of the entire domain $\sim \dfrac{l^2}{D}$. Therefore the boundary conditions for the Equation 15 would be:

$$
\begin{cases}
\lim_{r_d \to \infty} f(r_d) = 1 & \text{Flat} \\
\lim_{r_d \to r_{atom}} f(r_d) = \dfrac{l}{\kappa} & \text{Ramified}
\end{cases}
\tag{16}
$$

The form of the control function $f(r_d)$ is chosen to be a combination of linear and exponential terms as $f(r_d) = a r_d + b \exp(c r_d)$, from the boundary conditions in the Equation 16 one gets:

$$
f(r_d) = 1 + (\frac{l}{\kappa} - 1) \exp[-r_d]
\tag{17}
$$

Thus the feedback relaxation time t_{REL} is obtained as:

$$
t_{REL} = \frac{\kappa l}{D} \left(1 + (\frac{l}{\kappa} - 1) \exp[-r_d] \right)
\tag{18}
$$

The obtained feedback relaxation time t_{REL} is used as a control measure for real-time hampering of dendritic development, trend of which is schematically shown in the Figure 2b. The value of feedback relaxation time t_{REL} is highly sensitive to the radius of curvature r_d and hence changes in real time, while staying in the range of determined limits of $\dfrac{\kappa l}{D}$ and $\dfrac{l^2}{D}$.

The radius of curvature r_d can be approximated via the contours of the iso-potential curvature of the electric field in the vicinity of electrodeposits, where it occurs typically within the double layer region of thickness κ. The corresponding line could be obtained by allocating a magnitude of the iso-potential contour close-enough to the electrode ($V_{contour} := 0.9\Delta V$). The contour plot of MATLAB provides the iso-potential line with the specified value. If (x, y) represent the coordinates of the curvature line, the point of the minimum radius of curvature would address the most critical state, and requires higher dissipation of ionic concentration. The radius of curvature r_d can be calculated from Equation 19 as:

Var.	Value	Ref.
$\delta t(\mu s)$	1	[59]
$D(m^2/s)$	1.4×10^{-14}	[45]
$\#Li^+$	200	[45]
$\#Li^0$	400	[45]
$l(nm)$	167	[45]
$\Delta V(mV)$	85	[45]
Domain size	$16.7nm \times 16.7nm$	[45]

Table 1: Simulation parameters.

$$r_d = min\left\{ \left| \frac{\left(1 + \left(\frac{dy}{dx}\right)^2\right)^{\frac{3}{2}}}{\frac{d^2y}{dx^2}} \right| \right\}\Bigg|_{x=0}^{x=l} \tag{19}$$

This value is computed in real-time by means of finite difference and gets inserted into the feedback algorithm of the Figure 3. In fact, the curvature-dependent relaxation time provides a positive feedback for halting of the growing dendrites, which is negative feedback for dendritic evolution. The Flowchart 3 represents the control loop representing the real-time computation of the curvature and the corresponding feedback relaxation time for the minimization of the dendritic branching. Figure 2b schematically represents such variation where the feedback relation time t_{REL} starts from the minimum value of $\sim \frac{\kappa l}{D}$ in the flat surface and varies based on the measurement of the highest curvature of the tip given in the Equation 19.

The thickness of the double layer κ can be obtained from [54, 58, 60]:

$$\kappa = \sqrt{\frac{\varepsilon k_B T}{2z^2 e^2 C_\infty}} \tag{20}$$

where ε is the permittivity of the solvent, k_B is Boltzmann constant, T is the temperature, z is the valence number, e is the electron charge and C_∞ is the average ambient electrolyte concentration. Debye length by definition is the distance the charge electrostatic effect persists. Therefore in such region the concentrations are not uniform and the double layer forms in the same scale.

The computation was carried out based on the simulation parameters given in the Table 1. Figure 4 illustrates the resulted morphologies of the grown dendrites based on the applied relaxation time. It is clear that the higher rest period t_{OFF} generates more dense morphology. The most uniform deposition is resulted from the maximum value of rest period $t_{OFF} = \frac{l^2}{D}$ and with very close proximity from the optimized feedback relaxation time t_{REL}, given in the Equation 18.

The density of the electro-deposits can easily be calculated from confining the atoms in a rectangle, the height of which spans to the highest dendrite coordinates h. Therefore:
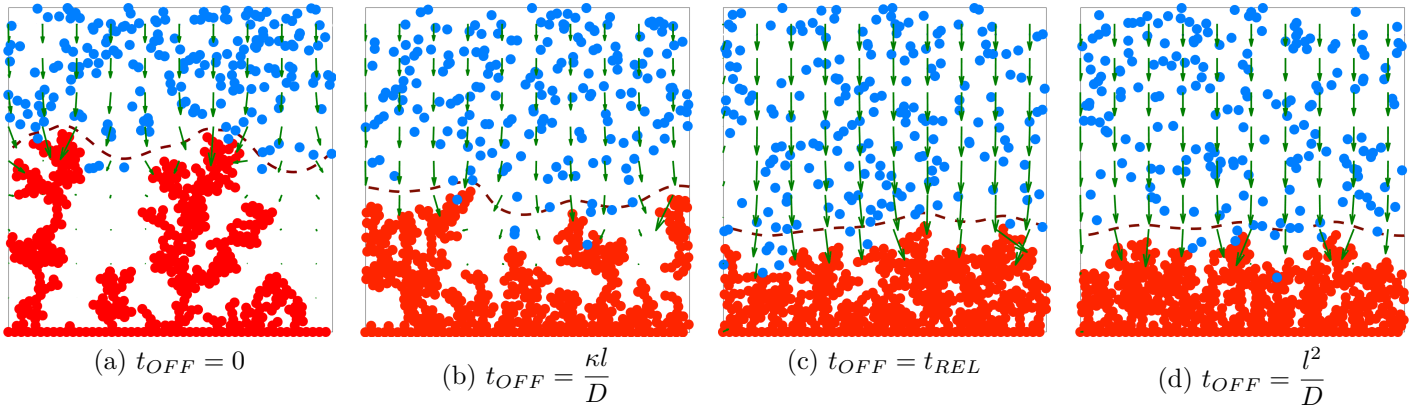
(a) $t_{OFF} = 0$ (b) $t_{OFF} = \dfrac{\kappa l}{D}$ (c) $t_{OFF} = t_{REL}$ (d) $t_{OFF} = \dfrac{l^2}{D}$

Figure 4: Ultimate morphologies obtained for different relaxation periods.

$$\rho = \frac{N \pi a^2}{hl}$$

where N is the number of atoms composing the dendrite, a is the atomic radius and l is the scale of the domain. The density of the morphologies, sample of which is shown in the Figure 6 is provided in the Figures 6a, 6b and 6c versus various relaxation time values as the control parameter and $N \in \{200, 400, 800\}$. In order to mitigate the steady-state condition, for every deposited atom, one extra atom is randomly added to the moving free ions.

Furthermore, the variation of the highest interfacial curvature (minimum radius of curvature r_d) and their corresponding feedback relaxation time t_{REL} and the density ρ versus the number of deposited atoms are shown in the Figures 7a, 7b and 7c.

3 Experimental

We performed experiments within a manually-fabricated sandwich cell [61], which provides the possibility of in-situ observation of growing dendrites from the periphery (Figure 5a). The cell encompasses two Li^0 disc electrodes ($d = 1.59cm$) with the distance of $L = 0.32cm$ via a transparent acrylic PMMA separator. The fabricated cells were filled with $0.4cm^3$ of $LiPF_6$ in a solution with stoichiometric compound of EC:EMC$\equiv$1:1 in an argon-filled glovebox ($H_2O, O_2 < 0.5ppm$). Multiple such cells were electrolyzed with the values given in the Table 2, generated by a programmable multichannel cycler. After the passage of $48mAh$ ($\approx 173C$) through the cells, 3 images within the periphery of 120^0 were taken by means of Leica M205FA optical microscope through the acrylic separator. The image processing algorithm is described as below:

1. The RGB image is read to the program by 3 values of $\{Red, Green, Blue\} \in [0, 255]$ and has been converted to a grayscale image I with individual values of range $I_{i,j} \in [0, 1]$.

2. The grayscale image $I_{i,j}$ is binarized to $J_{i,j}$ via the grayness threshold I_c as below:

$$J_{i,j} = \begin{cases} 1 & I_{i,j} \geq I_c \\ 0 & I_{i,j} < I_c \end{cases}$$

the threshold value I_c has been chosen to minimize the weighted intra-class variance σ^2 defined as:

$$\begin{cases} \sigma^2 = \omega_0 \sigma_0^2 + \omega_1 \sigma_1^2 \\ \omega_0 + \omega_1 = 1 \end{cases}$$

where ω_0 and ω_1 are the total fraction of element divided by the value of I_c and σ_0^2 and σ_1^2 are their respective variances. [62] Such minimization ensures that the resulted

3. The circular sandwich cell with the radius r has been divided of 3 arcs with the angle of $\dfrac{2\pi}{3}$ and width incremental length of δx, which is supposed to be projected to a 2D plane with the incremental width of $\delta x'$. From Figure 5a due to geometry we have: $x = \dfrac{d}{2}\sin(\theta)$, $\rightarrow dx = \dfrac{d}{2}\cos(\theta)d\theta$, where $\cos(\theta) = \sqrt{1 - \dfrac{4x^2}{d^2}}$; hence:

$$\delta x' = \frac{\delta x}{\sqrt{1 - \dfrac{4x^2}{d^2}}}$$

where d is diameter of the sandwich cell [63].

4. Starting from the electrode surface, the occupied space by the dendrites has been calculated by the square site percolation paradigm [64].

5. The infinitesimal calculations have been integrated and normalized to inter-electrode distance ($\hat{\lambda}_i := \lambda_i / l$) to get the dendrite measure $\bar{\lambda}$ as:

$$\begin{aligned}
\bar{\lambda} &= \frac{1}{\pi d l} \sum_{k=1}^{3} \int_{-\frac{\pi}{3}}^{+\frac{\pi}{3}} \hat{\lambda}_k(\theta) \frac{d}{2} d\theta \\
&= \frac{1}{\pi d l} \sum_{k=1}^{3} \int_{-\frac{\pi}{3}}^{+\frac{\pi}{3}} \frac{\hat{\lambda}_k(x) dx}{\sqrt{1 - \dfrac{4x^2}{d^2}}}
\end{aligned} \tag{21}$$

The integral Equation 21 has been obtained by incremental sum from experimental data. Figure 5b shows such investigation for the duty cycles of $\mathbf{D} = \{0.4, 0.8\}$, where the red encirclement is the approximated dendrite area, the green rectangle is the total area, and the red line represents the height of the tallest obtained dendrite in each experiment. The detailed experimental parameters are given in the Table 2.

Note that the current density i and the ionic flux j are correlated with $i = zFj$, where z is the valence number of charge carriers and $F = 96.5$ kC/mol is the Faraday's constant, representing the amount of charge per mole.
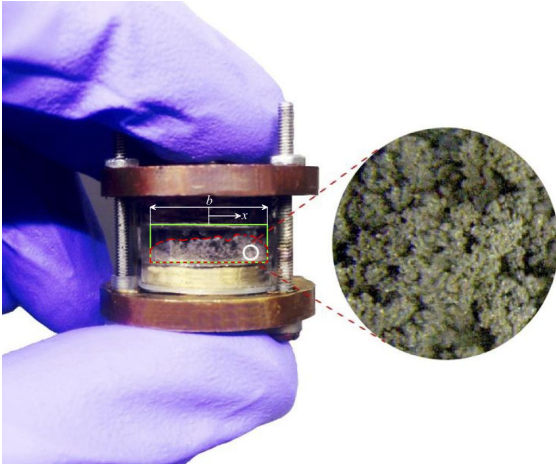
(a) Naked-eye observation of dendrites.[25]
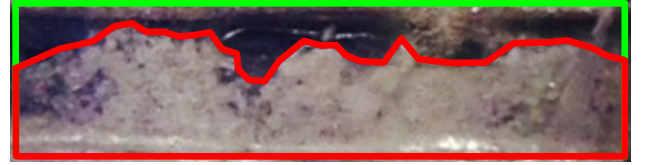
$\mathbf{D} = 0.8$, $\rho = 0.77$

$\mathbf{D} = 0.4$, $\rho = 0.34$

(b) Obtained fractional area of the morphologies (red enclosures) for $\mathbf{D} = 0.8$ (top) and $\mathbf{D} = 0.4$ (bottom) used for computing dendrite measure $\bar{\lambda}$.

Figure 5: Experimental Procedure.

Parameter	$\mathbf{D}$	i	l	r	T	C_∞	Q
Value	$\{0.4, 0.8\}$	1	3.175	7.95	298	1	173
Unit	[ ]	mA/cm^2	mm	mm	K	M	C

Table 2: Experimental Parameters.

4 Results & Discussion

The mechanism used in the pulse charging works based on the relaxation of the ionic concentration in the dendritic tips where the order of concentration is as follows:

$$\text{Concentration: } Tip > Bulk > Voids$$

The formation of such concentration gradient after the instigation, in fact, leads to the further growth. Therefore the applied feedback relaxation time should effectively dissipate away the accumulated ions from the concentrated regions. The sharper interfaces, which grow faster than the rest of the interface, have higher number of concentrated ions around them and therefore they are in the most critical state, which have been focused-on for the computation of the feedback relaxation time t_{REL}.

In the larger scale, the electro-migration displacement (Eq. 3) scales with $\sim t$ and the diffusion displacement (Eq. 2) scales with the square root of time $\sim \sqrt{t}$. During the pulse both electro-migration and diffusion are in action whereas during the rest period diffusion is the main drive. Since the average reach for electro-migration is higher than the sole-diffusion, the range of reach in the rest period should in fact be competitive with the pulse period. Therefore:

$$\sqrt{2Dt_{OFF}} \geq \mu \vec{\mathbf{E}} t_{ON} \pm \sqrt{2Dt_{ON}} \tag{22}$$

and performing further, we get the maximum value of duty cycle $\mathbf{D}$ for effective pulse charging:
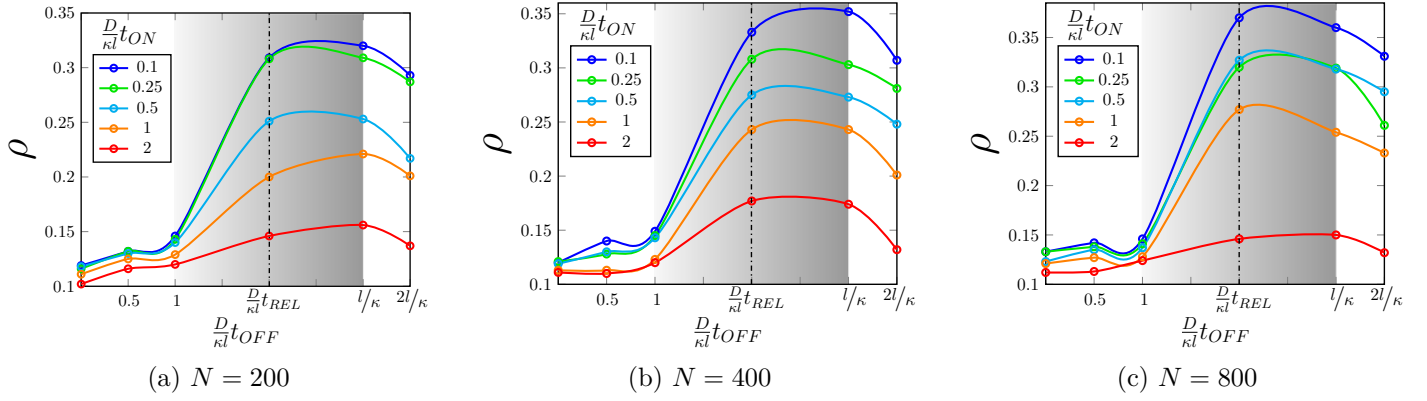
12

Figure 6: Density ρ variations versus dimension-less relaxation time $\frac{D}{\kappa l}t_{OFF}$ for different charge amount N.

$$\mathbf{D_{max}} = max\left(\frac{1}{\left(1 + \frac{|\vec{\mathbf{E}}|}{RT}\sqrt{\frac{D}{2f}}\right)^2 \pm 1}\right) \leq \frac{1}{2} \tag{23}$$

where the duty cycle of the $\frac{1}{2}$ is the limiting value for the effective suppression of dendrites which is achieved when the pulse frequency f gets indefinitely large (i.e. $f \to \infty$). This trend is visualized in the Figure 5b, where the $\mathbf{D} = 0.4$ shows very effective suppression, whereas the same charge amount with the $\mathbf{D} = 0.8$ does not relatively show efficacy for uniform growth.

The formation of local branches indicates that the concentration of ions in those specific sights is high and therefore those sites should be focus locations for the feedback relaxation time t_{REL}, which highly depends on their respective radius of curvature r_d [52]. For an individual ramified peak with the radius of curvature r_d, the time required for the concentration relaxation within the double layer t_{REL}^{DL} with the scale of $\sim \kappa$ is :

$$t_{REL}^{DL} \approx \frac{\kappa(\kappa + r_d)}{D} \ll \frac{\kappa l}{D} \tag{24}$$

where D is the diffusivity value for the ionic transport. The relaxation in the double layer with the scale of $\sim \kappa$ occurs locally and since the scale of the double layer is far less than the cell domain ($\kappa \ll l$), the relationship in the Equation 24 shows that the branched morphology has significantly faster relaxation rate relative to the flat surface ($t_{REL}^{DL} \ll \frac{\kappa l}{D}$) .

The concentration relaxation could occur wither in the local or global scale. Therefore for the scales extending to the entire cell domain (i.e. $\sim l$), the feedback relaxation time t_{REL} should be higher.

13

Considering the curvature of the interface, the scale of transport for the time and space would lead to the following comparison:

$$\frac{\kappa^2}{D} \leq t_{REL}^{DL} \leq \frac{\kappa l}{D} \leq t_{REL} \leq \frac{l^2}{D} \tag{25}$$

Hence the relaxation time scale varies from $\sim \frac{\kappa^2}{D}$ in the individual peaks to the $\sim \frac{l^2}{D}$ in the larger domain of the cell, and the control relaxation time in fact varies in such range. The density of the electro-deposits ρ shown in the Figure 6 correlates inversely with the pulse period t_{ON}. This is due to the exacerbated branching during the charge time which upon growing further gets more difficult to halt. Vice versa, the finer pulse period t_{ON} provides better possibility for the suppression of dendrites. Needless to mention that such pulse period t_{ON} could not indefinitely get short since the ions ultimately would require enough time to reach the dendrites during this time and transform from ionic to atomic species.

In addition, the density values ρ correlate with the relaxation time t_{OFF} until reaching a certain saturation limit. Since the length of the domain is much larger than the double layer ($l \gg \kappa$), the range of feedback relaxation time t_{REL}, shown by color gradient, would extremely reduce the charging time with negligible compensation in the density of electro-deposits ρ. The underlying reason is that the relaxation would let the ionic concentration to relax and uniform ionic distribution. Vice versa, extra relaxation period will not helpful since the ionic concentration is already relaxed and the concentration gradient has already vanished. The comparative density values based on the feedback relaxation time t_{REL} are in good agreement with the morphologies represented in the Figure 4.

The experimental data in the Figure 5 are higher values than the simulation results in the Figure 6. The underlying reason is the inclusion of the voids in the porous dendrites as the dendrite body.

Moreover, imposing higher-than-limit relaxation time would slightly reduce the density ρ since additional concentration from the ambient electrolyte could be depleted in the into the non-reacting dendritic sites. The atoms might excessively diffuse-in and therefore disturb the relaxed concentration, beyond equilibrium. The negligible increase in the density of the dendrites ρ in the span of Figures 6a, 6b and 6c illustrates the effective-ness of the pulse charging method for the multitudes of the charge amount N, which is the number of electro-deposited atoms.

The dendritic evolution can be divided into two distinctive stages of the transient and steady-state (S.S.) growth regimes [51, 65], which has been illustrated in the Figures 7a, 7b and 7c in real-time versus the deposited charge N. The initial transient regime in fact is stochastic in nature whereas the steady state regime can illustrate an effective trend. Figure 7a represents the variation of the radius of the curvature r_d in the growing interface versus the deposition progress N (i.e. number of the atoms). In this figure, the transition stage during the higher pulse time shows more fluctuation which indicates the non-uniform regime of growth for the augmented pulse intervals. On the other hand during the steady-state (S.S.) regime, radius of curvature correlates inversely with the pulse time interval t_{ON},
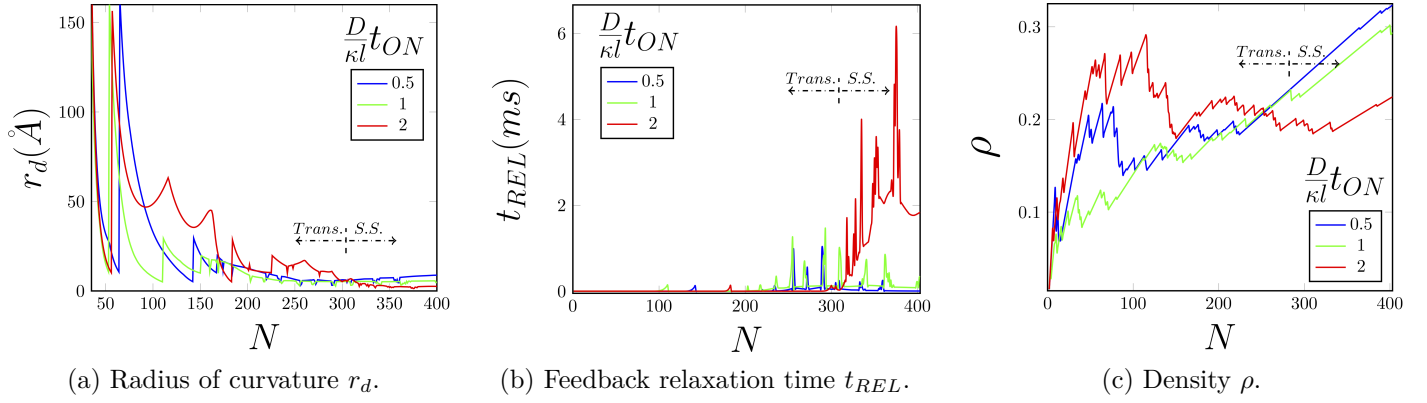
(a) Radius of curvature r_d.　　(b) Feedback relaxation time t_{REL}.　　(c) Density ρ.

Figure 7: Transient and steady-state behavior in the radius of curvature r_d, feedback relaxation time t_{REL} and the obtained density ρ based on the dimension-less pulse period $\frac{D}{\kappa l}t_{ON}$.

which indicates that the morphology is controlled for finer pulse periods.

Figure 7b represents the control relaxation time t_{REL} versus the progress in electrodeposition during the dendritic evolution, where the higher pulse intervals would require higher amount of control relaxation time t_{REL} for the effective suppression of the dendrites. Also, the higher fluctuation for the higher amount of pulse charge t_{ON} shows the higher control rate due to faster dynamics of variation in the curvature.

The same trend of transition-to-steady state regimes has been observed in the Figure 7c, where the highest fluctuation occurs for the higher pulsing time t_{ON} where it leads to the lowest density ρ after reaching the steady growth regime.

In fact, the increasingly fast growth regime of the dendrites illustrates that the larger height h of the electrodeposits, the higher the rate of their growth. This can simply be represented by the following:

$$\frac{dh}{dt} \propto h$$

where the integration leads to the exponential relationship for the growth regime as:

$$h(t) \propto \exp(bt)$$

where b is the coefficient of the proportion. Setting exponential relationship causes a very high sensitivity for the control relaxation time t_{REL} to act vigilantly to the smallest perturbation in the ramified peaks. The form of the control relation time t_{REL} proportionally contains the exponential form in Equation 18. Note that other forms of the relaxation time would as well could satisfy the boundary conditions given in the Equation 16 such as t_{REL}^{alt} below:

$$t_{REL}^{alt} \approx \frac{\kappa l}{D}\left(\frac{r_d + l}{r_d + \kappa}\right) \tag{26}$$

which has lower sensitivity for the radius of curvature r_d relative to proposed control relation time

t_{REL}. This can be proven by calculating their derivative with respect to radius of curvature ($\frac{dt_{OFF}}{dr_d}$) and show that:

$$\frac{dt_{REL}}{dr_d} \gg \frac{dt_{REL}^{alt}}{dr_d}$$

Thus from equations 18 and 26 and considering the negative value for both derivatives, one must have:

$$\frac{\kappa - l}{\kappa \exp(r_d)} \frac{\kappa l}{D} > \frac{\kappa - l}{(r_d + \kappa)^2} \frac{\kappa l}{D} \tag{27}$$

since $\kappa \ll l$ dividing by negative value of $\kappa - l$ changes the inequality sign, therefore:

$$\exp(r_d) > (r_d + \kappa)^2 \tag{28}$$

The equation 28 is obvious for a large values of radius of curvature r_d since the exponential term in the denominator will surpass the quadratic term in the right side. For an infinitesimally small value of the radius of curvature r_d one can use Taylor expansion as: $\exp(r_d) \approx 1 + r_d + \overset{0}{\cancel{O(r_d^2)}}$ and one has:

$$\kappa(1 + r_d) > (r_d + \kappa)^2$$

re-arranging gives:

$$r_d^2 + \kappa r_d + \kappa^2 - \kappa < 0$$

which is a quadratic equation in terms of the radius of curvature r_d and the root is found as:

$$r_d = \sqrt{\kappa - \frac{3}{4}\kappa^2} - \frac{\kappa}{2}$$

Considering the infinitesimal value for thickness of the double layer ($\kappa \to 0$) the value for r_d would be very small. Therefore for the most range of $r_d \in [r_{atom}, \infty)$ the exponential relationship given in the Equation 18 remains the most sensitive to the variations in the radius of curvature r_d as an effective control parameter for suppression of the dendrites..

In practice, the noticing the formation of a ramified peak in the dendrite morphology for potentiostatic charging (constant applied voltage V) could be obtained by discerning the sudden increase in the current density, whereas for galvanic charging (constant applied current I) could be the sudden drop in the potential value, where both of these events represent the runaway process (i.e. jump) in time.

Needless to mention that regardless of the utilized electrolyte, the comparative results are valid, since the existence of the electrolyte medium only slows down the ionic interactions to the same scale in both case scenarios.

5 Conclusions

In this paper we have developed an variable pulse relaxation method in real-time for the minimization of dendrites grown during electrodeposition. Our framework prevents the excessive branched evolution of the growing microstructures where the control parameter is considered as the maximum curvature of the interface. The corresponding feedback relaxation time t_{REL}, hence is a function of the radius of curvature where the sensitivity to the variation of radius is extremely hight by setting the exponential correlation. The density of the electrodeposites, which has been computed as the measure of uniformity for the morphologies, has been compared agains the traditional pulse-relaxation method. Both the density values and the presented morphologies indicate that the run-away dynamics upon the branching of the electrodeposits which has been controlled effectively by real-time tracking of the radius of curvature. The methodology has potential for utilization of smart charging in rechargeable batteries and controlling the morphology of the grown electro-deposits.

List of Symbols

N : Number of electrodeposits (i.e. charge amount)

$\delta\vec{\mathbf{r}}_D$: Diffusion displacement (m)

D : Diffusion coefficient of the electrolyte ($m^2.s^{-1}$)

$\vec{\mathbf{E}}$: Local electric field ($V.m^{-1}$)

$\delta\vec{\mathbf{r}}$: Total displacement of one ion (m)

f : Frequency of Pulse (s^{-1})

t_{ON} : Pulse period (s)

r_d : Radius of curvature (m)

l : Scale of the domain (m)

t_{REL} : Optimal rest period (s)

ε : the electrolyte permittivity ($C.V^{-1}.m^{-1}$)

k_B : Boltzmann constant ($kg.m^2.s^{-2}.K^{-1}$)

T : Temperature (K)

h : Highest dendrite y-coordinate (m)

I_c : Grayness threshold ([ ])

σ^2 : Intra-class variance ([ ])

ω_0 ; ω_1 : Fractions of $B\&W$ groups divided by I_c ([ ])

σ_0^2 ; σ_1^2 : Variances for ω_0 and ω_1 ([ ])

ρ: Density of the electrodeposits ([ ])

δt : Coarse time interval (s)

$\hat{\mathbf{g}}$: Unit vector in a random direction ([ ])

$\delta\vec{\mathbf{r}}_M$: Migration displacement (m)

V: Voltage (V)

P: Total period of pulse and rest (s)

$\mathbf{D}$: Duty cycle ([ ])

t_{OFF} : Rest period (s)

a: Atomic radius (m)

κ : Interfacial double layer thickness (m)

$f(r_d)$: Augmentation factor as a function of r_d ([ ])

z : Valence number ([ ])

e : Electron charge (C)

C_∞ : Average ambient electrolyte concentration ($mol.m^{-3}$)

$I_{i,j}$: Grayscale value ([ ])

$J_{i,j}$: Binarized grayscale value ([ ])

d : Diameter of the sandwich cell (m)

$\hat{\lambda}_i$: Normalized dendrite height ([ ])

t_{REL}^{DL} : Double layer relaxation time (s)

t_{REL}^{alt} : Alternative expression for the relaxation time (s)

Supplementary Materials

The supplementary materials with this publications is additionally included online as: **i.** The density of atomic clusters, **ii.** variation in the radius of curvature, relaxation period and the density with time.

Acknowledgement

Data Availability

The raw data required to reproduce these findings are available to download from http://dx.doi.org/10.17632/nzprv4bxrr.1. The processed data required to reproduce these findings are available to download from http://dx.doi.org/10.17632/fbhhy8gb8t.1.

References

[1] Moran Balaish, Alexander Kraytsberg, and Yair Ein Eli. A critical review on lithium air battery electrolytes. *Phys. Chem. Chem. Phys.*, 16(7):2801–2822, 2014.

[2] Rotem Marom, S Francis Amalraj, Nicole Leifer, David Jacob, and Doron Aurbach. A review of advanced and practical lithium battery materials. *Journal of Materials Chemistry*, 21(27):9938–9954, 2011.

[3] John B Goodenough and Kyu-Sung Park. The li-ion rechargeable battery: a perspective. *Journal of the American Chemical Society*, 135(4):1167–1176, 2013.

[4] Xieyu Xu, Yangyang Liu, Jang-Yeon Hwang, Olesya O Kapitanova, Zhongxiao Song, Yang-Kook Sun, Aleksandar Matic, and Shizhao Xiong. Role of li-ion depletion on electrode surface: Underlying mechanism for electrodeposition behavior of lithium metal anode. *Advanced Energy Materials*, 10(44):2002390, 2020.

[5] Si-e Sheng, Li Sheng, Li Wang, Nan Piao, and Xiangming He. Thickness variation of lithium metal anode with cycling. *Journal of Power Sources*, 476:228749, 2020.

[6] Ji Qian, Shuo Wang, Yu Li, Menglu Zhang, Fujie Wang, Yuanyuan Zhao, Qiang Sun, Li Li, Feng Wu, and Renjie Chen. Lithium induced nano-sized copper with exposed lithiophilic surfaces to achieve dense lithium deposition for lithium metal anode. *Advanced Functional Materials*, page 2006950, 2020.

[7] Tianhan Gao, Colton Rainey, and Wei Lu. Piezoelectric mechanism and a compliant film to effectively suppress dendrite growth. *ACS Applied Materials & Interfaces*, 2020.

[8] Yuan Wang, Hong-Qian Sang, Wenqi Zhang, Yuyang Qi, Rong-Xiang He, Bolei Chen, Weiwei Sun, Xing-Zhong Zhao, Dejun Fu, and Yumin Liu. Electrophoretic deposited black phosphorus on 3d porous current collectors to regulate li nucleation for dendrite-free lithium metal anodes. *ACS Applied Materials & Interfaces*, 2020.

[9] Zeeshan Ahmad, Zijian Hong, and Venkatasubramanian Viswanathan. Design rules for liquid crystalline electrolytes for enabling dendrite-free lithium metal batteries. *Proceedings of the National Academy of Sciences*, 117(43):26672–26680, 2020.

[10] Qizhang Yan, Grace Whang, Ziyang Wei, Shu-Ting Ko, Philippe Sautet, Sarah H Tolbert, Bruce S Dunn, and Jian Luo. A perspective on interfacial engineering of lithium metal anodes and beyond. *Applied Physics Letters*, 117(8):080504, 2020.

[11] Wei Huang, Yikang Yu, Zhen Hou, Zhuojian Liang, Yiyi Zheng, Zewei Quan, and Yi-Chun Lu. Dendrite-free lithium electrode enabled by graphene aerogels with gradient porosity. *Energy Storage Materials*, 33:329–335, 2020.

[12] Chunhui Gao, Kena Sun, Bo Hong, Kai Zhang, Zhian Zhang, and Yanqing Lai. Guided dendrite-free lithium deposition through titanium nitride additive in li metal batteries. *International Journal of Hydrogen Energy*, 45(53):28294–28302, 2020.

[13] Rui Wang, Jin Yu, Juntao Tang, Ruijin Meng, Linda F Nazar, Lezhi Huang, and Xiao Liang. Insights into dendrite suppression by alloys and the fabrication of a flexible alloy-polymer protected lithium metal anode. *Energy Storage Materials*, 32:178–184, 2020.

[14] W. Xu, J. L. Wang, F. Ding, X. L. Chen, E. Nasybutin, Y. H. Zhang, and J. G. Zhang. Lithium metal anodes for rechargeable batteries. *Energy and Environmental Science*, 7(2):513–537, 2014.

[15] Deepti Tewari, Sobana P Rangarajan, Perla B Balbuena, Yevgen Barsukov, and Partha P Mukherjee. Mesoscale anatomy of dead lithium formation. *The Journal of Physical Chemistry C*, 2020.

[16] Zhe Li, Jun Huang, Bor Yann Liaw, Viktor Metzler, and Jianbo Zhang. A review of lithium deposition in lithium-ion and lithium metal secondary batteries. *J. Power Sources*, 254:168–182, 2014.

[17] Asghar Aryanfar, Tao Cheng, and William A Goddard. Bulk properties of amorphous lithium dendrites. *ECS Transactions*, 80(10):365–370, 2017.

[18] Yaoyu Ren, Yang Shen, Yuanhua Lin, and Ce-Wen Nan. Direct observation of lithium dendrites inside garnet-type lithium-ion solid electrolyte. *Electrochemistry Communications*, 57:27–30, 2015.

[19] Christoffer P Nielsen and Henrik Bruus. Morphological instability during steady electrodeposition at overlimiting currents. *arXiv preprint arXiv:1505.07571*, 2015.

[20] PP Natsiavas, K Weinberg, D Rosato, and M Ortiz. Effect of prestress on the stability of electrode–electrolyte interfaces during charging in lithium batteries. *Journal of the Mechanics and Physics of Solids*, 95:92–111, 2016.

[21] J. Steiger, D. Kramer, and R. Monig. Mechanisms of dendritic growth investigated by in situ light microscopy during electrodeposition and dissolution of lithium. *J. Power Sources*, 261:112–119, 2014.

[22] N. Schweikert, A. Hofmann, M. Schulz, M. Scheuermann, S. T. Boles, T. Hanemann, H. Hahn, and S. Indris. Suppressed lithium dendrite growth in lithium batteries using ionic liquid electrolytes: Investigation by electrochemical impedance spectroscopy, scanning electron microscopy, and in situ li-7 nuclear magnetic resonance spectroscopy. *J. Power Sources*, 228:237–243, 2013.

[23] Reza Younesi, Gabriel M Veith, Patrik Johansson, Kristina Edstrom, and Tejs Vegge. Lithium salts for advanced lithium batteries: Li-Metal, Li-O2, and Li-S. *Energy and Environmental Science*, 8(7):1905–1922, 2015.

[24] GM Stone, SA Mullin, AA Teran, DT Hallinan, AM Minor, A Hexemer, and NP Balsara. Resolution of the modulus versus adhesion dilemma in solid polymer electrolytes for rechargeable lithium metal batteries. *J. Electrochem. Soc.*, 159(3):A222–A227, 2012.

[25] Asghar Aryanfar, Tao Cheng, Agustin J Colussi, Boris V Merinov, William A Goddard III, and Michael R Hoffmann. Annealing kinetics of electrodeposited lithium dendrites. *The Journal of chemical physics*, 143(13):134701, 2015.

[26] Asghar Aryanfar, Daniel J Brooks, AgustÃn J Colussi, Boris V Merinov, William A Goddard III, and Michael R Hoffmann. Thermal relaxation of lithium dendrites. *Phys. Chem. Chem. Phys.*, 17(12):8000–8005, 2015.

[27] Yuanzhou Yao, Xiaohui Zhao, Amir A Razzaq, Yuting Gu, Xietao Yuan, Rahim Shah, Yuebin Lian, Jinxuan Lei, Qiaoqiao Mu, Yong Ma, et al. Mosaic rgo layer on lithium metal anodes for effective mediation of lithium plating and stripping. *Journal of Materials Chemistry A*, 2019.

[28] Ji Qian, Yu Li, Menglu Zhang, Rui Luo, Fujie Wang, Yusheng Ye, Yi Xing, Wanlong Li, Wenjie Qu, Lili Wang, et al. Protecting lithium/sodium metal anode with metal-organic framework based compact and robust shield. *Nano Energy*, 2019.

[29] Wei Deng, Wenhua Zhu, Xufeng Zhou, Fei Zhao, and Zhaoping Liu. Regulating capillary pressure to achieve ultralow areal mass loading metallic lithium anodes. *Energy Storage Materials*, 2019.

[30] Alexander W Abboud, Eric J Dufek, and Boryann Liaw. Implications of local current density variations on lithium plating affected by cathode particle size. *Journal of The Electrochemical Society*, 166(4):A667–A669, 2019.

[31] Markus Klinsmann, Felix E Hildebrand, Markus Ganser, and Robert M McMeeking. Dendritic cracking in solid electrolytes driven by lithium insertion. *Journal of Power Sources*, 442:227226, 2019.

[32] Chen Xu, Zeeshan Ahmad, Asghar Aryanfar, Venkatasubramanian Viswanathan, and Julia R Greer. Enhanced strength and temperature dependence of mechanical properties of li at small scales and its implications for li metal anodes. *Proceedings of the National Academy of Sciences*, 114(1):57–61, 2017.

[33] Guangyu Liu, Dandan Wang, Jianyu Zhang, Andrew Kim, and Wei Lu. Preventing dendrite growth by a soft piezoelectric material. *ACS Materials Letters*, 1(5):498–505, 2019.

[34] Peng Wang, Wenjie Qu, Wei-Li Song, Haosen Chen, Renjie Chen, and Daining Fang. Electro–chemo–mechanical issues at the interfaces in solid-state lithium metal batteries. *Advanced Functional Materials*, page 1900950, 2019.

[35] Rangeet Bhattacharyya, Baris Key, Hailong Chen, Adam S Best, Anthony F Hollenkamp, and Clare P Grey. In situ nmr observation of the formation of metallic lithium microstructures in lithium batteries. *Nat. Mater.*, 9(6):504, 2010.

[36] S Chandrashekar, Nicole M Trease, Hee Jung Chang, Lin-Shu Du, Clare P Grey, and Alexej Jerschow. 7li mri of li batteries reveals location of microstructural lithium. *Nat. Mater.*, 11(4):311–315, 2012.

[37] Yunsong Li and Yue Qi. Energy landscape of the charge transfer reaction at the complex li/sei/electrolyte interface. *Energy & Environmental Science*, 2019.

[38] Laleh Majari Kasmaee, Asghar Aryanfar, Zarui Chikneyan, Michael R Hoffmann, and AgustÃn J Colussi. Lithium batteries: Improving solid-electrolyte interphases via underpotential solvent electropolymerization. *Chem. Phys. Lett.*, 661:65–69, 2016.

[39] S Chandrashekar, Onyekachi Oparaji, Guang Yang, and Daniel Hallinan. Communication 7li mri unveils concentration dependent diffusion in polymer electrolyte batteries. *Journal of The Electrochemical Society*, 163(14):A2988–A2990, 2016.

[40] Asghar Aryanfar, Daniel J Brooks, and William A Goddard. Theoretical pulse charge for the optimal inhibition of growing dendrites. *MRS Advances*, 3(22):1201–1207, 2018.

[41] J. N. Chazalviel. Electrochemical aspects of the generation of ramified metallic electrodeposits. *Phys. Rev. A*, 42(12):7355–7367, 1990.

[42] Xin Zhang, Q Jane Wang, Katharine L Harrison, Katherine Jungjohann, Brad L Boyce, Scott A Roberts, Peter M Attia, and Stephen J Harris. Rethinking how external pressure can suppress dendrites in lithium metal batteries. *Journal of The Electrochemical Society*, 166(15):A3639–A3652, 2019.

[43] V. Fleury. Branched fractal patterns in non-equilibrium electrochemical deposition from oscillatory nucleation and growth. *Nature*, 390(6656):145–148, 1997.

[44] Deepti Tewari and Partha P Mukherjee. Mechanistic understanding of electrochemical plating and stripping of metal electrodes. *Journal of Materials Chemistry A*, 7(9):4668–4688, 2019.

[45] Asghar Aryanfar, Daniel Brooks, Boris V. Merinov, William A. Goddard Iii, Agustin J. Colussi, and Michael R. Hoffmann. Dynamics of lithium dendrite growth and inhibition: Pulse charging experiments and Monte Carlo calculations. *The Journal of Physical Chemistry Letters*, 5(10):1721–1726, 2014.

[46] Wenyu Mu, Xunliang Liu, Zhi Wen, and Lin Liu. Numerical simulation of the factors affecting the growth of lithium dendrites. *Journal of Energy Storage*, 26:100921, 2019.

[47] David R Ely, Aniruddha Jana, and R Edwin GarcÃa. Phase field kinetics of lithium electrodeposits. *J. Power Sources*, 272:581–594, 2014.

[48] Daniel A Cogswell. Quantitative phase-field modeling of dendritic electrodeposition. *Physical Review E*, 92(1):011301, 2015.

[49] Rohan Akolkar. Mathematical model of the dendritic growth during lithium electrodeposition. *J. Power Sources*, 232:23–28, 2013.

[50] Martin Z Bazant, Brian D Storey, and Alexei A Kornyshev. Double layer in ionic liquids: Over-screening versus crowding. *Phys. Rev. Lett.*, 106(4):046102, 2011.

[51] Peng Bai, Ju Li, Fikile R Brushett, and Martin Z Bazant. Transition of lithium growth mechanisms in liquid electrolytes. *Energy & Environmental Science*, 9(10):3221–3229, 2016.

[52] Asghar Aryanfar, Michael R Hoffmann, and William A Goddard III. Finite-pulse waves for efficient suppression of evolving mesoscale dendrites in rechargeable batteries. *Physical Review E*, 100(4):042801, 2019.

[53] M. S. Chandrasekar and M. Pushpavanam. Pulse and pulse reverse plating - conceptual, advantages and applications. *Electrochim. Acta*, 53(8):3313–3322, 2008.

[54] Martin Z Bazant, Katsuyo Thornton, and Armand Ajdari. Diffuse-charge dynamics in electrochemical systems. *Physical review E*, 70(2):021506, 2004.

[55] Jean Philibert. One and a half century of diffusion: Fick, einstein, before and beyond. *Diffusion Fundamentals*, 4(6):1–19, 2006.

[56] Philip J Pritchard, John W Mitchell, and John C Leylegian. *Fox and McDonald's Introduction to Fluid Mechanics, Binder Ready Version*. John Wiley & Sons, 2016.

[57] Raymond A Serway and John W Jewett. *Physics for scientists and engineers with modern physics*. Cengage learning, 2018.

[58] Robert J Hunter. *Foundations of colloid science*. Oxford university press, 2001.

[59] Ron O Dror, Morten Ø Jensen, David W Borhani, and David E Shaw. Exploring atomic resolution physiology on a femtosecond to millisecond timescale using molecular dynamics simulations. *Journal of General Physiology*, 135(6):555–562, 2010.

[60] Johannes Lyklema. *Fundamentals of interface and colloid science: soft colloids*, volume 5. Elsevier, 2005.

[61] Asghar Aryanfar. Method and device for dendrite research and discovery in batteries, April 11 2017. US Patent 9,620,808.

[62] Nobuyuki Otsu. A threshold selection method from gray-level histograms. *Automatica*, 11(285-296):23–27, 1975.

[63] Asghar Aryanfar, Daniel J Brooks, Agustin J Colussi, and Michael R Hoffmann. Quantifying the dependence of dead lithium losses on the cycling period in lithium metal batteries. *Phys. Chem. Chem. Phys.*, 16(45):24965–24970, 2014.

[64] Asghar Aryanfar, William Goddard III, and Jaime Marian. Constriction percolation model for coupled diffusion-reaction corrosion of zirconium in pwr. *Corrosion Science*, 158:108058, 2019.

[65] G. Gonzalez, M. Rosso, and E. Chassaing. Transition between two dendritic growth mechanisms in electrodeposition. *Physical Review E*, 78(1), 2008.